

Contents

Abstract	i
Abstract in lingua italiana	iii
Contents	v
Introduction	1
1 Nuclear structure and deformations	5
1.1 Nuclear structure models	5
1.1.1 Phenomenology of the NN interaction	6
1.1.2 Structure models	7
1.2 Nuclear pairing	12
1.3 Nuclear deformations	12
1.3.1 Quadrupole deformation	13
1.3.2 Nilsson model	15
1.3.3 Octupole deformations and parity breaking	17
1.4 Nuclear fission	18
1.4.1 Symmetry breaking and microscopic approaches to fission	21
2 State of the art, objectives and methods	25
2.1 State of the art and motivation	25
2.2 State of the Art	25
2.2.1 Basis expansion methods	26
2.2.2 Symmetry-Restricted mesh methods	26
2.2.3 Unconstrained Coordinate-Space (Mesh) Methods	27
2.2.4 Towards more efficient unconstrained methods	27
2.3 Objectives	28
2.4 Methods	28

3 Energy functional	31
3.1 Hartree-Fock theory	31
3.1.1 Variational principle	31
3.1.2 Hartree-Fock equations	32
3.1.3 Symmetries in Hartree-Fock	34
3.1.4 Density Functional Theory	36
3.2 Pairing in Hartree-Fock theory	37
3.2.1 BCS theory	38
3.2.2 Hartree-Fock-Bogoliubov theory	40
3.3 Skyrme	44
3.3.1 Skyrme force	44
3.3.2 Energy density functional	46
3.3.3 Functionals	50
3.4 Coulomb interaction	50
3.5 Energy calculation	51
4 Numerical methods	55
4.1 Finite differences	55
4.1.1 3D mesh	55
4.1.2 Schrödinger equation	56
4.1.3 Poisson equation	58
4.2 Eigenvalue problem	59
4.2.1 Conjugate Gradient and numerical techniques	60
4.2.2 Iterative eigensolvers	64
4.2.3 Generalized Conjugate Gradient	67
4.3 Code implementation details	69
4.3.1 Constraints	69
4.3.2 Details on the implementation of the code	71
4.3.3 Optimal parameters choice	71
4.3.4 Numerical stability	73
5 Results for spherical nuclei	77
5.1 Physical quantities	77
5.1.1 Mean square radii	77
5.2 Parameters and mesh choice	78
5.3 Results for ^{16}O	78
5.3.1 Results neglecting Coulomb interaction	79
5.4 Results for heavier nuclei	81

5.4.1	Comparison with experimental binding energies	81
6	Results for deformed nuclei	87
6.1	^{24}Mg Benchmarks	87
6.1.1	Deformation parameters	87
6.1.2	HFBTHO code and calculation details	88
6.1.3	EV8 code and calculation details	90
6.1.4	EV8 code comparison	91
6.2	Other results	91
6.2.1	Deformation curve for different functionals	92
Bibliography		95
A Appendix		105
A.1	Spherical harmonics	105
A.1.1	Algorithm	106
A.2	5-point derivatives	106
A.3	Functional derivatives	106
A.4	\bar{U} , \bar{V} matrix structure	108
List of Figures		109
List of Tables		111
List of Symbols		113
Acknowledgements		115

Introduction

The theoretical study of atomic nuclei provides a bridge between nuclear physics and nuclear engineering. Starting from a framework consistent with quantum mechanics, the strong interaction, and its underlying symmetries, modern nuclear theory aims to construct models characterized by a limited number of free parameters and capable of predicting both nuclear structure and reactions across a wide range of systems. While experimental data have long provided invaluable insight into nuclear properties and processes, only a coherent theoretical description allows for systematic extrapolations toward regions of the nuclear chart or physical conditions that remain beyond current experimental reach, thus playing an essential role in applications relevant to nuclear engineering.

In particular, nuclear fission, despite its massive importance in nuclear engineering, remains only partially understood from a microscopic standpoint. Current models that use empirical approaches [59, 61], successfully reproduce global quantities like fission barrier heights, fragment mass distributions, and average neutron multiplicities for well studied nuclei. However, these models may rely on a huge number of parameters, which limit their predictive power when extrapolated to systems which are less investigated experimentally. A fully microscopic understanding of the collective dynamics leading from the compound nucleus to scission, the treatment of quantum many-body correlations [76], and the description of fragment excitation and emission remain among the major open challenges, particularly relevant for the simulation of next-generation reactors, which require the accurate description of nuclei and fuel materials – far less explored than those employed in traditional thermal systems – to be correctly predicted.

In this regard, the approach to the microscopic description of nuclei, is the one of the many-body theory, which starting from the interacting nucleons, aims at building a complete description of the nucleus. The use of phenomenological potentials based on the Woods-Saxon one is still relevant, thanks to its computational feasibility and its capability to include shell effects in a simple manner, but it cannot account for many-body effects. At the moment, there are two competing frameworks that try to tackle the microscopic description of nuclei,

i the *ab-initio* approach [41], where the interaction is in principle exact, derived from controlled approximations of quantum chromodynamics; and

ii the use of effective interactions and nuclear Density Functional Theory[3, 27].

Ab-initio methods, while technically speaking more rigorous, are still limited as of now, since they can only account for light nuclei or medium-heavy nuclei that can be considered as spherical. Energy density functionals and effective interactions, such as the Skyrme force, on the other hand are more flexible and less computationally expensive, enabling a much wider representation of nuclei across the whole chart, including heavy nuclei and processes such as fission, fusion, reactions and decays, which are of crucial importance in nuclear engineering.

D Vautherin and D M Brink laid the foundations of the nuclear Hartree-Fock theory using the Skyrme interaction in 1972 [88], through spherically symmetric calculations, which are unable to account for nuclear deformations, essential for nuclei far from magic numbers. Over the years, thanks to the increase in computational performance of modern hardware, codes that are able to represent more coordinates have been written, mainly using basis expansions on the harmonic oscillator [56, 77], which have the downside of not being able to account for near drip line nuclei, due to the different asymptotic behavior of the Gaussian basis in the harmonic oscillator and quasi-resonant states.

In the past twenty years, the use of Cartesian meshes to better account for such extremal cases has been introduced [14, 24, 58, 73], often times assuming certain approximations, such as plane reflection symmetries [72] and axial symmetry [58]. The use of fully unconstrained Hartree-Fock methods, of critical importance for exotic deformations, is still a novel endeavour that only a handful of implementations have tackled, due to the high computational cost.

The aim of this work is to explore a new computational approach, the Generalized Conjugate Gradient method, to efficiently solve spatially unconstrained Skyrme functionals. This thesis is organised as follows:

- In chapter 1, a short, comprehensive introduction to nuclear physics and its open problems is given, as to prime the reader on the essential physical properties of atomic nuclei, starting from phenomenological facts and empirical models. A formal description of nuclear deformations and fission is also given, to highlight the importance of symmetry breaking.
- In chapter 2, the motivations and objectives of this work are presented, along with a summary of the methods used to achieve them.

- In chapter 3, the theoretical framework used in the present work is reviewed, by introducing aspects of Hartree-Fock theory, Density Functional Theory and the effective interaction used in this work.
- In chapter 4, the numerical methods used in this work are presented, along with actual implementations in writing the code.
- In chapter 5, results for the spherically symmetric case are presented as a way of benchmarking the new implementation of this thesis, along with a description of the main physical quantities we compare.
- In chapter 6, benchmarks for the deformed nucleus ^{24}Mg are shown, after which novel results regarding... are presented.

1 | Nuclear structure and deformations

In this chapter, a concise introduction to nuclear structure physics is provided, as a way to understand the essential physical quantities, terminology, and phenomenology of atomic nuclei to then have the necessary background to tackle nuclear deformations within the microscopic framework in later sections. The reader may refer to introductory textbooks on nuclear physics, such as ref. [9, 63] for a more in-depth treatment of the subject and ref. [69] for a focus on many-body theory.

This chapter is organised as follows, first, in section 1.1, we will review the main empirical facts about nuclides, such as particle density distribution, binding energies and phenomenological models employed to describe them. Moving on to more advanced topics, that are able to complete the general description of nuclear structure, which are nuclear pairing in section 1.2 and nuclear deformations in section 1.3. Lastly, in section 1.4, we will review the nuclear fission process, derive a simple model to describe it, and discuss the importance of deformations to accurately describe it.

1.1. Nuclear structure models

The study of low energy hadron physics, has always been a challenging task. This is due to the known fact that the strong force, which is responsible for the interaction between nucleons, is not perturbative at low energies, as opposed to the atomic case for the Coulomb interaction, whose coupling can be assumed as constant at low energies, while the one for the strong interaction cannot. Nevertheless, both problems have in common the fact that they are related to many-body theory, thanks to which they share some challenges and the corresponding solutions, when present.

1.1.1. Phenomenology of the NN interaction

It is possible to obtain a good insight on nuclear structure, by using empirical data obtained experimentally on the bulk properties of nuclei, such as the binding energy and the particle density.

Binding energies

Let us start with the binding energy. We can define it as the mass defect of the nucleus with respect to the constituents – protons and neutrons – isolated from each other. If Z is the number of protons, N the number of neutrons, and $A = N + Z$ the nuclear mass, then the binding energy E_B is given by

$$E_B = (Zm_p + Nm_n - M)c^2, \quad (1.1)$$

where m_p is the proton mass, m_n the neutron mass, and M the nucleus mass.

In figure 1.1, the binding energy per nucleon E_B/A as a function of A is presented. As shown in the figure, the binding energy per nucleon rapidly saturates and stalls around 7 MeV just after $A = 4$, this striking behaviour is due to nucleons interacting only with near neighbours, since the strong force is a short-range interaction. Otherwise, the trend would follow a behaviour similar to $\sim (A-1)$ as in the Coulomb interaction case, meaning the binding energy per nucleon would be linear with the mass number.

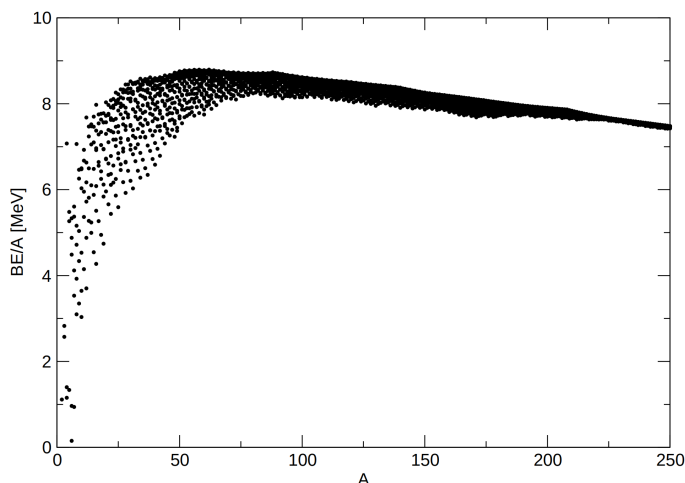


Figure 1.1: Binding energy per nucleon as a function of A . Due to the short range of the strong force, this value saturates around 7 MeV, with a steady, dim decrease after ^{56}Fe . Figure taken from [27].

Nuclear density

An important aspect of nuclear phenomenology that can be accessed experimentally is the nuclear density, most notably through elastic electron-nucleus scattering [42]. The measured form factor can be related to the Fourier transform of the charge density, from which the spatial distribution is reconstructed. The resulting densities are well reproduced by a Fermi-like distribution of the form

$$\rho(r) = \frac{\rho_0}{1 + e^{(r-R_0)/a}}, \quad (1.2)$$

where R_0 is the nuclear radius, which can be parametrized as $R_0 \approx 1.2A^{1/3}$, and a is the diffusivity, whose value determines how sharp the density drops from its saturation value $\approx \rho_0$ to ≈ 0 . The saturation density ρ_0 is generally universal for all nuclei, amounting to $\approx 0.16 \text{ fm}^{-3}$.

1.1.2. Structure models

The theoretical description of nuclear structure has been proven to be a difficult task over the years. Due to the extremely rich phenomenology of nuclei and the challenges brought by the strong force, as we shall see, many models and further approximations to give a satisfactory description of all nuclides have been proposed.

Liquid drop model

One, if not the first successful model, is the liquid drop model. It is based on the assumption that the nucleus behaves as a liquid droplet, where forces among constituents saturate. This hypothesis, formulated by G. Gamow, culminated in the formalization of the semi-empirical mass formula (SEMF) by N Bohr and C F von Weizsäcker in 1935 [89], which reads

$$E_B = a_V A - a_S A^{2/3} - a_C \frac{Z(Z-1)}{A^{1/3}} - a_A \frac{(N-Z)^2}{A} + \delta_P \quad (1.3)$$

where E_B is the binding energy of the nucleus. Each term has a different physical meaning:

- $a_V A$ is the volume energy of the nucleus, given by the approximately constant binding energy per nucleon, which makes the total energy proportional to A ;
- $a_S A^{2/3}$ is the surface energy, a correction to the volume energy due to outer nucleons interacting with fewer nucleons than those in the inner bulk, meaning that a_S is of the same order of a_V ;
- $a_C Z(Z-1)/A^{1/3}$ is the approximation to the Coulomb energy repulsion of the

nucleus, assuming the protons are uniformly distributed;

- $a_A(N - Z)^2/A$ is the asymmetry energy, which is due to the Pauli exclusion principle, since protons and neutrons occupy their respective states, a high imbalance of one species or the other implies loosely bound nucleons, thus a higher energy contribution of those states; and
- $\delta_P = a_P A^{-1/2}$ refers to the pairing contribution, due to the increase in binding energy of an even number of neutrons and/or protons, more details on the pairing energy are given in section 1.2.

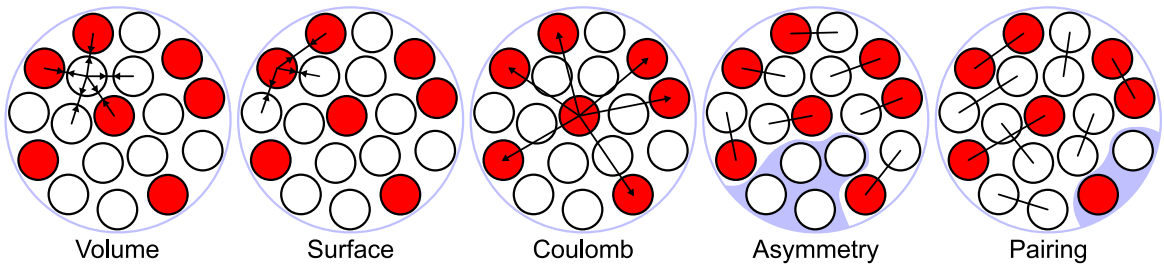


Figure 1.2: Visual representation of the liquid drop model. Figure taken from [35].

The SEMF can be fitted on experimental data to get a good estimate of binding energies [6], but it still lacks the ability of describing many aspects of nuclear structure, mainly, the nuclear shell structure, which can account for magic numbers and nuclear deformations.

An example of the SEMF parametrization is given in table 1.1, values are taken from [70].

Coefficient	a_V	a_S	a_C	a_A	a_P
Value [MeV]	15.8	17.8	0.711	23.7	11.2

Table 1.1: A typical parametrization of the coefficients in the SEMF (1.3). Values from [70].

Shell corrections

The liquid drop model, while being a good approximation for the description of the nuclear binding energy, it only accounts for the Pauli exclusion principle and the saturation of the strong force, providing only a partial description of the full quantum mechanical nature of the nucleus, thus the need to account for shell effects. Unfortunately, unlike the ‘atomic’

case, there is no single source of the field to which nucleons are subject to, since it's generated by the nucleons themselves; nonetheless, the formulation of an empirical mean-field potential which reproduces experimental data has been proven to be successful in providing useful corrections.

The so called Woods-Saxon potential is an empirical field used for modelling the average field to which an independent nucleon would feel in a nucleus. It is formulated as to follow the shape of the nuclear density (1.2), and it reads

$$U(\mathbf{r}) = -\frac{U_0(A, N)}{1 + e^{\frac{r-R}{a}}}, \quad (1.4)$$

where U_0 is the potential depth

$$U_0(A, N) = U_0 \left(1 \pm \kappa \frac{2N - A}{A} \right), \quad (1.5)$$

and the $+$ and $-$ signs refer to protons and neutrons respectively. R refers to the radius of the nuclear surface, parametrized as

$$R = r_0 A^{1/3} \quad (1.6)$$

and a is the surface diffuseness, as in the density expression (1.2).

Spin-orbit coupling The success of the shell model is mainly due to the possibility of accounting for spin-orbit coupling, which is included through a term that reads

$$U_{LS}(\mathbf{r}) = U_0^{LS} \left(\frac{r_0}{\hbar} \right)^2 \frac{1}{r} \frac{d}{dr} \left(\frac{1}{1 + e^{\frac{r-R}{a}}} \right). \quad (1.7)$$

A typical parametrization of the values in the Woods-Saxon potential and the spin-orbit term is given in table 1.2, values are taken from [79].

U_0 [MeV]	κ	r_0 [fm]	a [fm]	U_0^{LS} [MeV·fm ²]
52.1	0.639	1.260	0.662	22.0

Table 1.2: Typical Woods-Saxon potential parameters. Values from [79].

As shown in table 1.2, the spin-orbit coupling strength is high, compared to the atomic case, this causes a bigger splitting of the energy levels, leading to the formation of stable closed shells when the magic numbers 8, 20, 28, ... are reached, as shown in figure 1.3.

Coulomb interaction In the spherical case, the coulomb interaction can be taken as the energy potential produced by a sphere of charge Z and radius R , which reads

$$U_C(r) = Ze^2 \begin{cases} \frac{3-(r/R)^2}{2R} & r \leq R, \\ \frac{1}{r} & r > R. \end{cases} \quad (1.8)$$

The complete Hamiltonian then reads

$$\hat{H} = \hat{T} + U + U_{\text{LS}} + U_C, \quad (1.9)$$

where U_C is present only when solving for the proton shells. The solution to the eigenvalue problem $\hat{H}\psi = E\psi$ is of the form

$$\psi_{nljm_j} = \frac{u_{nl}(r)}{r} [Y_{nl}(\hat{\mathbf{r}}) \otimes \chi_{1/2}]_{jm_j} \quad (1.10)$$

where $Y_{nl}(\hat{\mathbf{r}})$ is the spherical harmonic function of degree l and order m , the $\hat{\mathbf{r}}$ notation is used to denote dependence on the azimuthal and polar angles of \mathbf{r} , the symbol \otimes takes the meaning of the angular momentum coupling with the spinor $\chi_{1/2}$, and $u_{nl}(r)$ satisfies the reduced Schrödinger equation

$$\left(-\frac{\hbar^2}{2m} \frac{d^2}{dr^2} + \frac{\hbar l(l+1)}{2mr^2} + U(r) \right) u_{nl} = Eu_{nl}. \quad (1.11)$$

The effect of the spin-orbit coupling U_{LS} and the Coulomb repulsion U_C could be accounted for by using first order perturbation theory.

Harmonic oscillator

A small digression on the harmonic oscillator is in order. The solution of the spherical potential

$$U_{\text{HO}}(\mathbf{r}) = \frac{1}{2}m\omega^2 r^2, \quad (1.12)$$

produces the spherical harmonic oscillator basis, which is very similar to the basis one would get solving for the Woods-Saxon potential, provided that ω is taken as $41/A^{1/3}$ MeV. As a matter of fact, the harmonic oscillator basis is often used to perform calculations in nuclear physics. We will see in section 4.3 that a harmonic oscillator basis is used as starting guess for the numerical solution of a Woods-Saxon potential.

Shell structure

A graphical representation of the shells for a harmonic oscillator is shown in figure 1.3, where the contribution of the spin-orbit coupling is also accounted for; compared to the atomic case, shells whose total angular momentum is higher are lowered in energy, viceversa for lower total angular momentum, due to the sign of the spin-orbit coupling U_0^{LS} of $U_{\text{LS}}(\mathbf{r})$ in equation (1.7).

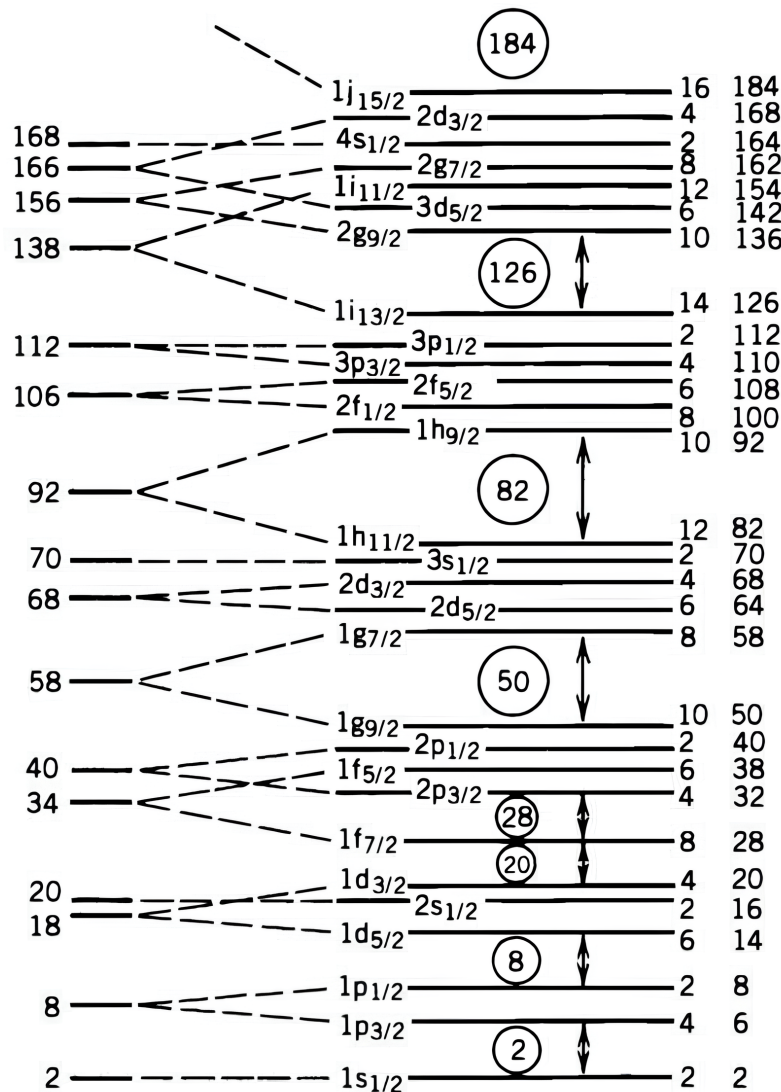


Figure 1.3: Graphical representation of a harmonic oscillator shells, together with the spin-orbit coupling. Shells whose total angular momentum is higher are lowered in energy, viceversa for lower total angular momentum. Figure adapted from [36].

1.2. Nuclear pairing

In the semi-empirical mass formula (1.3), the δ_p term can be parametrised as

$$\delta_p = \begin{cases} +\delta_0 & \text{if } N \text{ and } Z \text{ are even,} \\ 0 & \text{if } A \text{ is odd,} \\ -\delta_0 & \text{if } N \text{ and } Z \text{ are odd,} \end{cases} \quad (1.13)$$

hence having an even number of neutrons and/or protons increases the binding energy of the nucleus. A common choice for δ_0 is

$$\delta_0 = a_P A^{-1/2} \text{ MeV.}$$

A typical value for a_P is reported in table 1.1. This is a phenomena closely related to superconductivity, as nucleons of the same type form pairs that lie in higher energy states. An experimental evidence of this fact is known as odd-even staggering, where the separation energy

$$S_n = E_B(A+1, Z) - E_B(A, Z), \quad (1.14)$$

is higher for even A , an increase that corresponds to the energy necessary to break a pair. A graphical representation of the odd-even staggering for Sn isotopes is shown in figure 1.4. We will see in section 3.2 the two main methods to account for pairing at a microscopic level.

1.3. Nuclear deformations

If we were to observe the ratio between the first and second excited states energies of even-even nuclei, respectively $E(2^+)$ and $E(4^+)$, we would find that for nuclei where both N and Z are far from magic numbers, the ratio could be well approximated as

$$\frac{E(4^+)}{E(2^+)} \approx 3.33. \quad (1.15)$$

The ratio (1.15) can be explained by the collective rotation of the nucleus, when rotational symmetry is broken. Denoting by J the total angular momentum of this rotation, the quantized rotor energy reads

$$E_{\text{rot}} = \frac{\hbar^2}{2I} J(J+1), \quad (1.16)$$

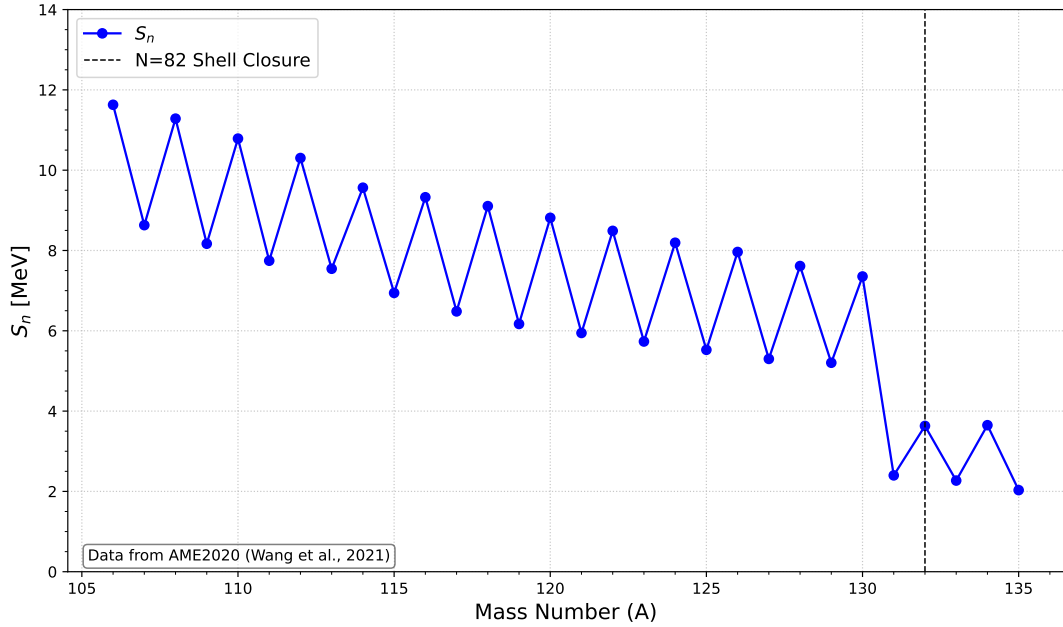


Figure 1.4: Odd-even staggering for Sn isotopes. Data taken from [1].

where \mathcal{I} is the nuclei's moment of inertia. Taking the ratio of equation (1.16) when $J = 4$ and $J = 2$, yields

$$\frac{20}{6} \approx 3.33. \quad (1.17)$$

Since there are many nuclei that display this property, it becomes obvious that nuclear deformations play a central role in the description of nuclear structure; as such, we shall now give a description of the nuclear shape in a formal framework. We will start by expanding the nuclear radius in terms of spherical harmonics and develop the case of an axial deformation. After that, we will briefly discuss the more general case of triaxial, octupole, and parity breaking configurations.

1.3.1. Quadrupole deformation

Let us suppose to consider variations of the nuclear radius R in terms of spherical harmonics

$$R(\theta, \phi) = R_0 \left[1 + \sum_{\lambda\mu} \alpha_{\lambda\mu} Y_{\lambda\mu}(\theta, \phi) \right], \quad (1.18)$$

where the moments $\alpha_{\lambda\mu}$, defined as

$$\alpha_{\lambda\mu} = \int Y_{\lambda\mu}^*(\theta, \phi) R(\theta, \phi) d\Omega \quad (1.19)$$

are considered small, in the sense that $|\alpha_{\lambda\mu}|^2 \ll |\alpha_{\lambda\mu}|$, so that the volume of the system

$$V = \iint_0^{R(\theta,\phi)} R^2 dR d\Omega = \frac{4}{3}\pi R_0^3 \left[1 + \frac{3}{4\pi} \sum_{\lambda\mu} |\alpha_{\lambda\mu}|^2 \right] \quad (1.20)$$

is conserved. Since Y_{00} is constant, including it in the expansion changes the total volume (1.20), we then set $\alpha_{00} = 0$. If we consider only frames of reference where the nucleus has a center of mass fixed at the origin, we get vanishing $\alpha_{1\mu}$ coefficients.

Now, let us consider only $\alpha_{2\mu}$ coefficients and neglect higher order terms, so that the deformation is purely quadrupolar, then the radius reads

$$R(\theta, \phi) = R_0 \left[1 + \sum_{\mu=-2}^2 \alpha_{2\mu} Y_{2\mu}(\theta, \phi) \right]. \quad (1.21)$$

If we assume to be in the reference frame in which the inertia tensor, proportional to the coefficients $\alpha_{2\mu}$, is diagonal, which is called intrinsic frame, then the sum

$$\alpha_{21} Y_{21}^* + \alpha_{2-1} Y_{2-1}^*$$

vanishes. Since R is a real valued function, we have the relation

$$\alpha_{\lambda\mu} Y_{\lambda\mu} + \alpha_{\lambda-\mu} Y_{\lambda-\mu} = 2 \operatorname{Re}\{\alpha_{\lambda\mu} Y_{\lambda\mu}\}, \quad (1.22)$$

as a consequence, the resulting expansion reads

$$\begin{aligned} R(\theta, \phi) &= R_0 \left[1 + a_{20} Y_{20} + 2 \operatorname{Re}\{a_{22} Y_{22}\} \right] \\ &= R_0 \left[1 + \sqrt{\frac{5}{16\pi}} \left(a_{20}(3 \cos^2 \theta - 1) + 2a_{22}\sqrt{3} \sin^2 \theta (\cos^2 \phi - \sin^2 \phi) \right) \right]. \end{aligned} \quad (1.23)$$

If we perform the substitution

$$a_{20} = \beta \cos(\gamma) \quad (1.24)$$

$$a_{22} = \beta \sin(\gamma) \quad (1.25)$$

and express the variation of R along the cartesian axes, we get

$$R_x - R_0 = \delta R_x = \sqrt{\frac{5}{4\pi}} \beta R_0 \cos \left(\gamma - \frac{2\pi}{3} \right), \quad (1.26)$$

$$R_y - R_0 = \delta R_y = \sqrt{\frac{5}{4\pi}} \beta R_0 \cos \left(\gamma + \frac{2\pi}{3} \right), \quad (1.27)$$

$$R_z - R_0 = \delta R_z = \sqrt{\frac{5}{4\pi}} \beta R_0 \cos \gamma. \quad (1.28)$$

Assuming the value of β to always be positive, in the case $\gamma = 0$, $\delta R_x = \delta R_y < \delta R_z$, meaning the nucleus is in a *prolate* configuration; while in the case of $\gamma = \pi/3$, $\delta R_x = \delta R_y > \delta R_z$, meaning the nucleus has an *oblate* shape. A general convention is to write β with a negative sign in the oblate case, and a positive sign in the prolate case.

By using trigonometric identities, it is trivial to show that unique shapes are found only for $\gamma \in [0; \pi/3]$, if γ takes a value different from 0 or $\pi/3$, the shape is said to be triaxial, meaning $\delta R_z \neq \delta R_x \neq \delta R_y$, the nucleus has no more rotational symmetries and is only symmetric for reflections along the (x, y) , (x, z) and (y, z) planes, which also induces parity symmetry.

1.3.2. Nilsson model

To understand the effect on single-particle motion of a deformed potential, we can consider the case of an axially deformed harmonic oscillator potential, for which $\omega_z \neq \omega_x = \omega_y = \omega_{\perp}$, meaning the oscillator frequency takes on a different value on the z axis than in the x and y axes.

To treat the deformation perturbatively, we can assume that the various frequencies deviate from the unperturbed $\omega_0 = 41/A^{1/3}$ MeV, in which case they may read

$$\omega_z = \omega_0 - \frac{2}{3}\varepsilon, \quad (1.29)$$

$$\omega_{\perp} = \omega_0 + \frac{1}{3}\varepsilon, \quad (1.30)$$

this definition of the frequencies satisfies the conservation of volume, at lowest order in ε , assumed to hold for

$$\omega_0^3 = \omega_z \omega_{\perp}^2. \quad (1.31)$$

We can thus write the single-particle Hamiltonian in the deformed potential as

$$H = H_0 + \varepsilon H_1, \quad (1.32)$$

$$H_0 = -\frac{\hbar^2}{2m} \nabla^2 + \frac{1}{2} m \omega_0^2 r^2, \quad (1.33)$$

$$\varepsilon H_1 = \frac{1}{3} \omega_0^2 \varepsilon (x^2 + y^2 - 2z^2) = -\frac{1}{3} \sqrt{\frac{16\pi}{5}} m \omega_0^2 \varepsilon r^2 Y_{20}. \quad (1.34)$$

H_0 is the usual spherical harmonic potential, for which the eigenfunctions, expressed through the usual quantum numbers $|nljm_j\rangle$ are known. Assuming ε to be small, we can evaluate the first order correction of H_1 to the system, which reads

$$\Delta E = \langle nljm_j | \varepsilon H_1 | nljm_j \rangle, \quad (1.35)$$

$$= -\frac{1}{3} \sqrt{\frac{16\pi}{5}} \varepsilon m \omega_0^2 \int r^2 u_{nl}(r) \langle jm_j | Y_{20} | jm_j \rangle dr, \quad (1.36)$$

$$= \frac{\varepsilon}{6} m \omega_0^2 \int r^2 u_{nl}(r) \frac{3m_j^2 - j(j+1)}{j(j+1)} dr, \quad (1.37)$$

thus in the limit of large j , states with the maximum total angular momentum projection m_j are shifted upwards, while states with the minimum m_j are shifted downwards; moreover, eigenstates with $\pm m_j$ are degenerate, as expected by the reflection symmetry of the Hamiltonian if the z axis is inverted.

Adding further empirical terms to reproduce experimental data, and the spin-orbit coupling, results in the formulation of the Nilsson model [60]. In figure 1.5, a graphical representation of the energy levels in the Nilsson model is shown [91].

Deformed Woods-Saxon

Recent studies of deformed nuclei have been carried out using empirical potentials such as deformed Woods-Saxon potentials [32, 44]. In these models, the nuclear shape is expanded as

$$R(\theta) = R_0 \left[1 + \sum_{\lambda}^L \beta_{\lambda} Y_{\lambda 0} \right], \quad (1.38)$$

so that the solution is axially symmetric and the problem is reduced to just the (r, θ) coordinates, in which we can write the potential as

$$U_{WS}(r, \theta) = -\frac{U_0(A, N)}{1 + e^{\frac{r-R(\theta)}{a}}}. \quad (1.39)$$

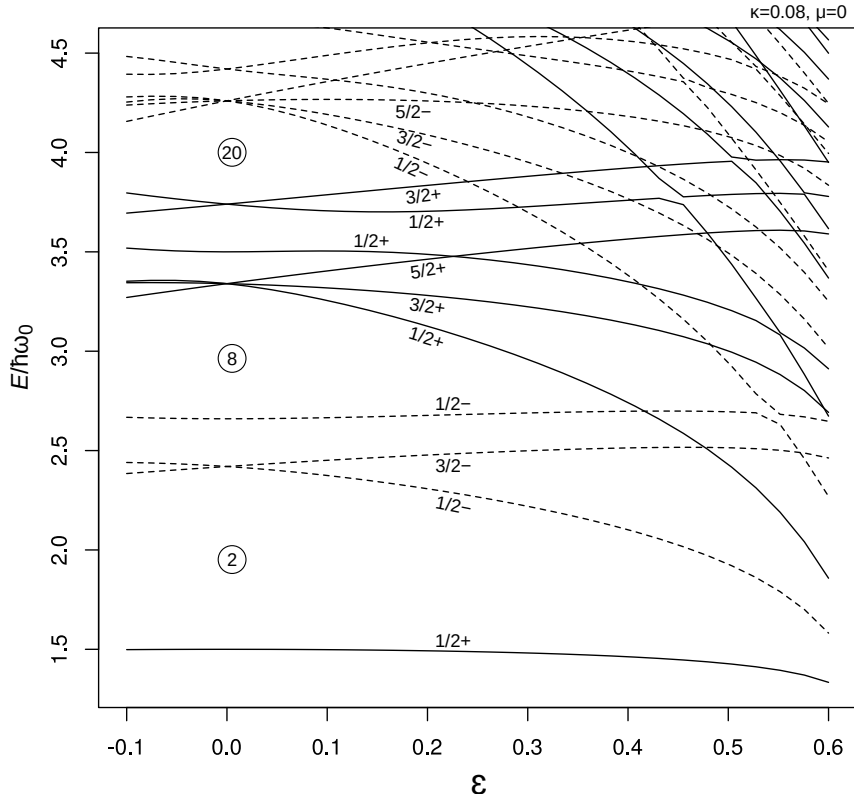


Figure 1.5: Nilsson model energy levels trends, as a function of ε . Figure taken from [91].

1.3.3. Octupole deformations and parity breaking

While quadrupole deformations concern nuclei across the whole chart, octupole deformations are much less common, being found in ground states only for heavier nuclei. The evidence for such deformations is mainly provided by the large electric octupole transition probability $B(E3)$, which reads

$$B(E3; 3^- \rightarrow 0^+) = \frac{1}{2J_i + 1} |\langle 0^+ | e r^3 \hat{Q}_3 | 3^- \rangle|^2, \quad (1.40)$$

where J_i is the initial total angular momentum of the nucleus and \hat{Q}_3 is the octupole operator defined as

$$\hat{Q}_3 = r^3 Y_{30}(\hat{r}). \quad (1.41)$$

Evidence of such strong coupling was initially found in neutron-rich Barium isotopes, ^{144}Ba [17] and ^{146}Ba [18], and a while later in Radium isotopes [20] and other heavy nuclei as well [19].

Expansions on spherical harmonics, under the parity operation $\mathcal{P} : \mathbf{r} \mapsto -\mathbf{r}$, transform as

$$\mathcal{P}\alpha_{\lambda\mu} = (-1)^\lambda \alpha_{\lambda\mu}, \quad (1.42)$$

hence a nuclear octupole deformation, whose order $\lambda = 3$, would break the parity symmetry of the mean-field. In figure 1.6 a graphical representation of the spherical harmonics for $\lambda = 3$ and $\mu = 0, 2$ is shown.



Figure 1.6: Graphical representation of possible octupole deformations. On the left, the axially symmetric Y_{30} deformation, on the right, the non-axial octupole deformation Y_{32} .

1.4. Nuclear fission

Nuclear fission is the process by which a nucleus splits into two – sometimes three – nuclei, whether spontaneously or when induced by a reaction. The physics that governs nuclear fission is that of a many-body, large-amplitude collective mode that gradually elongates the nuclear shape until the so-called *fission barrier* is surmounted and the energetically favoured path leads the nucleus to fragment. In figure 1.7, a graphical representation of the fission path and corresponding barrier is shown.

Although the basic idea of a nucleus dividing into two pieces may appear simple, the underlying dynamics is remarkably rich and involves several stages. Historically, the first theoretical interpretation of fission was given by Bohr and Wheeler in 1939 [12], who formulated the liquid-drop model description and introduced the concept of the fission barrier, determined by the competition between Coulomb repulsion and surface

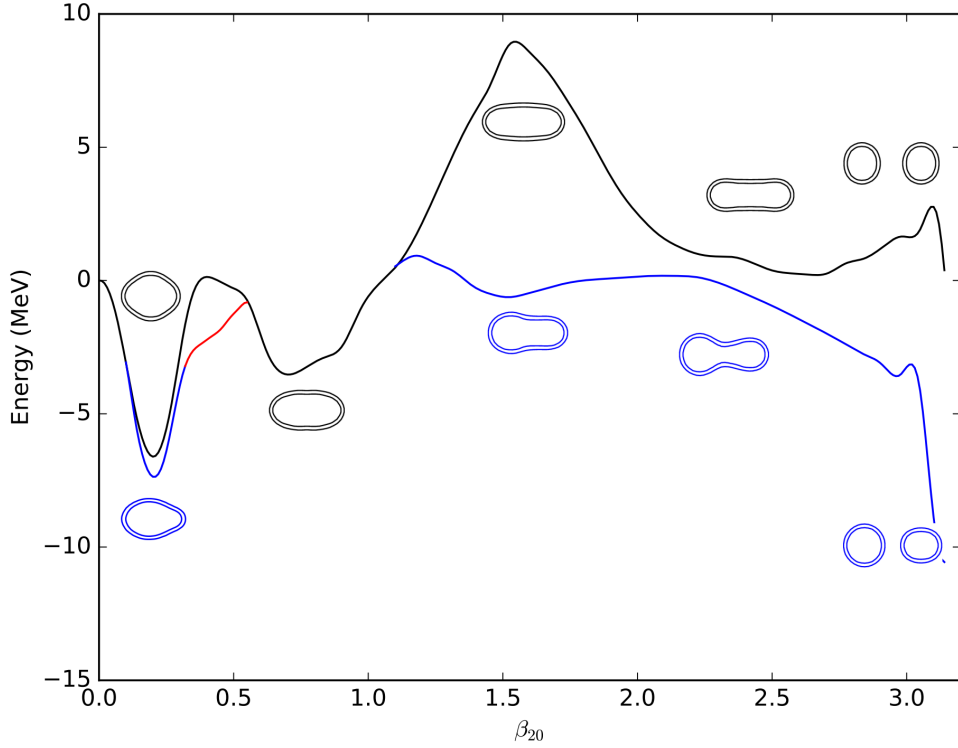


Figure 1.7: Fission path of ^{226}Ra , blue lines indicate axial octupole configurations, black lines indicate axial quadrupole and parity conserving configurations, red lines indicate triaxial, parity conserving configurations.

tension. Their framework already suggested that nuclei may experience intermediate configurations, multiple saddle points, and shape isomerism along the fission path.

Subsequent developments incorporated more detailed descriptions of the collective degrees of freedom and the role of shell effects, leading to the recognition that the fission landscape is often characterised by multiple barriers, intermediate minima, and highly deformed transition states [15, 87]. Modern microscopic approaches, based on energy-density functionals, have further clarified that fission dynamics involves a sequence of slow, dissipative shape evolutions, interspersed with possible gamma-decay pathways, and culminating in the formation of two (or more) pre-fragments connected by a narrowing neck. As the system evolves beyond the outer saddle, exotic spatial configurations appear, and the fragments themselves may exhibit deformation or even reflection asymmetry before scission. A visual representation of the overall fission process is shown in figure 1.8.

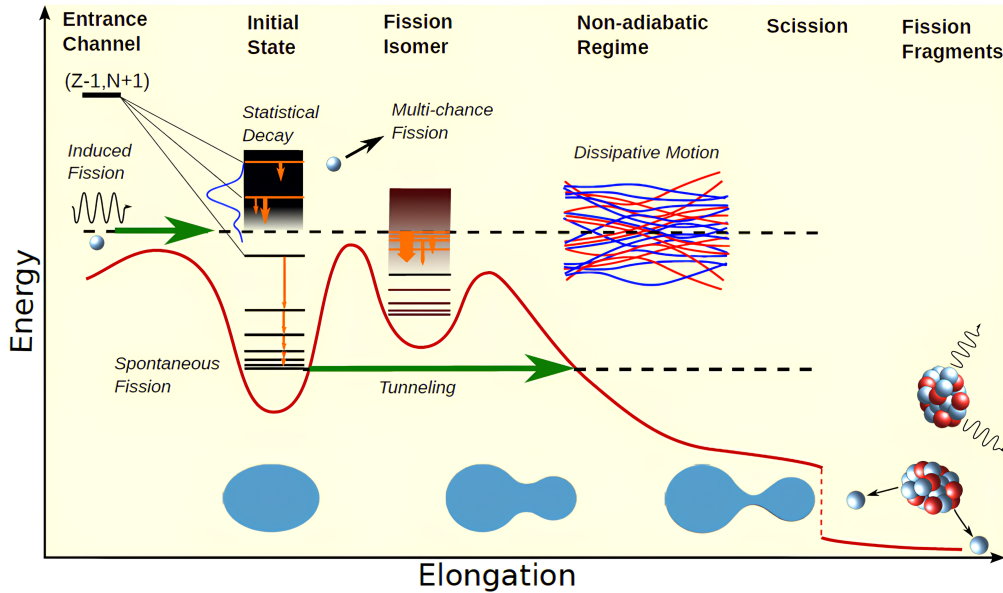


Figure 1.8: Visual representation of the fission process. Figure taken from [5].

Spontaneous fission model

It should be obvious that a formal treatment of deformations and collective modes is necessary to give a theoretical description of fission reactions. We can derive a simple spontaneous fission model by studying the effect of an axial quadrupole deformation on the semiempirical mass formula 1.3.

Let us assume that the nuclear radius may be expanded, as previously done in section 1.3, as

$$R = R_0[1 + \alpha_{20}Y_{20}]. \quad (1.43)$$

Assuming the nuclear volume is conserved across the fission path, the volume energy will not change. As for the surface energy, its variation can be expressed at the lowest order in α_{20} as

$$\Delta E_{\text{surf}} = E_{\text{surf}} - E_{0,\text{surf}} = E_{0,\text{surf}} \frac{2}{5} \alpha_{20}^2. \quad (1.44)$$

Regarding the Coulomb energy, the variation is given by

$$\Delta E_{\text{coul}} = E_{\text{coul}} - E_{0,\text{coul}} = -E_{0,\text{coul}} \frac{1}{5} \alpha_{20}. \quad (1.45)$$

Since the neutron and proton numbers does not change, the surface and Coulomb energies are the only contributions to the total energy difference. We can write

$$\Delta E = \frac{2}{5} \alpha_{20}^2 a_s A^{2/3} - \frac{1}{5} \alpha_{20}^2 a_c Z^2 A^{-1/3}, \quad (1.46)$$

if we set equation (1.46) to zero, we get, other than the undeformed solution for $\alpha_{20} = 0$,

$$\frac{Z^2}{A} = \frac{2a_s}{a_c}, \quad (1.47)$$

where the ratio $2a_s/a_c$ amounts to ≈ 50 in typical parametrizations of the SEMF. Equation (1.46), shows that for values of the so called *fissility parameter* Z^2/A larger than 50, the energy change becomes negative, favouring a configuration in which the nucleus fragments due to the spontaneous fission.

1.4.1. Symmetry breaking and microscopic approaches to fission

Microscopic theory

The use of phenomenological macroscopic-microscopic models has long provided valuable insight into fission processes, allowing for the prediction of barrier heights and fragment yields through parametrised shape degrees of freedom and empirical shell corrections [11, 16, 49]. In these models, the total energy is expressed as

$$E_{\text{tot}}(\mathbf{q}) = E_{\text{LD}}(\mathbf{q}) + \delta E_{\text{shell}}(\mathbf{q}) + \delta E_{\text{pair}}(\mathbf{q}), \quad (1.48)$$

where E_{LD} is the macroscopic liquid-drop term depending on deformation coordinates \mathbf{q} , while δE_{shell} and δE_{pair} account for shell and pairing corrections, respectively. While such models reproduce many global observables, they lack a true microscopic foundation. In particular, the collective coordinates \mathbf{q} are not derived from the underlying many-body dynamics, and the empirical shell corrections cannot describe the self-consistent rearrangement of the mean field along the fission path.

A more fundamental understanding is achieved within self-consistent mean-field approaches such as the Hartree-Fock or Hartree-Fock-Bogoliubov formalisms. The use of nuclear Density Functional Theory [3, 76] allows one to define a universal EDF $E[\rho, \kappa]$ that encapsulates both mean-field and pairing correlations. The resulting constrained HFB calculations produce the potential energy surface (PES) $E(\mathbf{q})$, mapping the energy of the system as a function of collective deformations such as the quadrupole (Q_{20}), octupole (Q_{30}), and triaxial (Q_{22}) moments. The minima and saddle points of this multidimensional PES determine the fission barriers and shape isomeric states [31, 78].

However, static mean-field approaches are limited by their single-reference character: the HFB vacuum represents only one configuration at a time, typically corresponding to a local minimum of the PES. In the vicinity of the fission barrier, where several configurations

with different intrinsic quantum numbers coexist, this approximation breaks down. The wave function should instead be expressed as a superposition of several self-consistent configurations $\{|\Phi(\mathbf{q})\rangle\}$, leading to a correlated state of the form

$$|\Psi\rangle = \int f(\mathbf{q}) |\Phi(\mathbf{q})\rangle d\mathbf{q}, \quad (1.49)$$

which is the essence of the *Generator Coordinate Method* (GCM) [38, 67]. The GCM maps the microscopic many-body problem onto a *collective Schrödinger equation* (CSE)

$$\left[-\frac{\hbar^2}{2} \sum_{ij} \frac{\partial}{\partial q_i} B_{ij}(\mathbf{q}) \frac{\partial}{\partial q_j} + V(\mathbf{q}) \right] g_k(\mathbf{q}) = E_k g_k(\mathbf{q}), \quad (1.50)$$

where $B_{ij}(\mathbf{q})$ is the collective inertia tensor and $V(\mathbf{q})$ the potential energy extracted from constrained HFB. This framework naturally incorporates tunnelling through the barrier and provides access to observables such as fission lifetimes and fragment distributions.

Beyond-mean-field extensions also restore symmetries that are spontaneously broken at the mean-field level. For instance, particle-number, parity, and angular-momentum projection techniques [4, 75] are required to recover good quantum numbers and remove spurious symmetry mixing. In multi-reference DFT [3], these symmetry restorations can be combined with configuration mixing, yielding highly accurate fission barrier calculations.

Unconstrained Calculations and Symmetry Breaking

An equally important aspect of microscopic fission theory is the treatment of spatial symmetries. Historically, many calculations imposed constraints such as axial symmetry or reflection symmetry with respect to a plane to reduce the computational cost of solving the HFB equations. While such restrictions simplify the description of the nucleus, they artificially constrain the fission path and may even prevent the identification of energetically preferred configurations [8, 90], as shown in figure 1.7. Fission involves strongly deformed, triaxial, and reflection-asymmetric shapes; the correct description of barrier heights and scission configurations therefore requires breaking as many spatial symmetries as possible.

In the self-consistent mean-field framework, spontaneous symmetry breaking is a feature rather than a flaw: it allows the system to adopt a deformed intrinsic shape corresponding to a broken rotational or parity symmetry, while the symmetry of the total many-body Hamiltonian is preserved. For example, an axially deformed HFB state violates rotational invariance, but the restoration of this symmetry through angular-momentum projection

recovers the correct laboratory-frame properties. Similarly, parity breaking through octupole deformation is essential to describe asymmetric fission fragment distributions. Triaxiality, for example, has been shown to lower the inner barrier of actinides by several MeV [78, 90]. Likewise, reflection-asymmetric (octupole) degrees of freedom are necessary to reproduce mass-asymmetric fission in heavy nuclei.

Recent computational developments have made possible fully symmetry-unrestricted HFB and TDDFT calculations, in which all spatial and time-reversal symmetries can be broken if energetically favourable [78, 81]. Codes such as HFODD and Sky3D implement three-dimensional solvers capable of describing triaxial, octupole, and time-odd components of the density matrix. These advances have revealed new fission pathways, scission configurations, and fragment-spin correlations inaccessible to axially symmetric models.

In summary, microscopic theories based on DFT and its extensions offer a self-consistent foundation for the description of nuclear fission. They provide direct access to the interplay between shell effects, pairing, and deformation, which determine the shape evolution from the ground state to scission.

2 | State of the art, objectives and methods

2.1. State of the art and motivation

The need to account for nuclear deformations has been highlighted already as a central theme in chapter 1, particularly in the context of heavy nuclei and of the complex fission dynamics discussed in section 1.4. Without allowing for deformation, several key features of nuclear systems – such as the excitation spectrum when rotational bands are present – cannot be captured, and limiting the description to only a subset of shapes often proves inadequate, as seen in the case of heavy nuclei in section 1.3. Similar limitations arise in dynamical processes and nuclear reactions, where shape evolution plays an essential role.

The central issue in nuclear structure theory is that the Hamiltonian is not known exactly and must be approximated. At the same time, the problem is inherently a many-body one, which remains computationally demanding, requiring approximations to make calculations tractable. Symmetry assumptions such as spherical or axial symmetry have therefore been widely used in numerical implementations to simplify the calculations and reduce computational cost. However, these constraints become insufficient in situations where deformation is a defining aspect of the system.

With the increasing availability of computational power and the development of modern numerical techniques, the field is now in a position to move beyond these restrictive assumptions. This motivates the development of new codes capable of treating the many-body problem without imposed symmetries, allowing the full range of nuclear deformations to emerge naturally from the underlying theory.

2.2. State of the Art

The approaches to the nuclear many-body problem can be broadly divided into two families: (a) *basis expansion methods*, which represent single-particle states in truncated har-

monic oscillator bases, and (b) *coordinate-space (mesh) methods*, which discretize space directly. In the following sections, we review these two classes of methods and motivate the need for more flexible and computationally efficient unconstrained solvers.

2.2.1. Basis expansion methods

Basis expansion approaches are among the most widely used techniques for solving the HF and HFB equations. In these methods, single-particle wavefunctions are expanded on a finite HO basis, chosen for its completeness and qualitative similarity to the mean-field potential of bound nuclei, as explained in section 1.1. Codes such as `HFBTHO`, also used in this work for benchmarking our implementation in section 6.1.2, are based on this framework.

The HO basis, however efficient, introduces structural limitations. First, weakly bound and continuum-like states, crucial for nuclei near the drip lines, are poorly represented because their asymptotic behavior differs fundamentally from that of HO functions. Whereas HO states decay as e^{-r^2} , quasi-bound states decay as e^{-r} , leading to slow convergence and difficulties in describing halos, neutron skins, and quasi-resonant states [30, 85]. Second, large deformations in heavy nuclei may require many HO shells to reproduce the stretched spatial geometry, significantly increasing the computational cost. The computational complexity grows rapidly with the maximum number of oscillator shells used in the calculation, resulting in demanding memory and CPU requirements for strongly deformed configurations [56].

In summary, despite their efficiency for near-spherical and moderately deformed nuclei, basis-expansion methods become inadequate for describing nuclei near drip lines, far from stability and largely deformed.

2.2.2. Symmetry-Restricted mesh methods

A second major class of HF/HFB solvers uses a spatial mesh as the variational space. Historically, fully unconstrained three-dimensional meshes were computationally prohibitive, which motivated the introduction of *symmetry constraints* to reduce the dimensionality of the problem. By enforcing specific spatial symmetries, the number of degrees of freedom is greatly reduced, making coordinate-space calculations tractable on available hardware.

The most common choices are spherical and axial symmetry. Spherical HF/HFB solvers [26, 88] reduce the equations to a radial problem, achieving excellent computational efficiency and precision for the structure of spherical or near-spherical nuclei. Axially sym-

metric solvers [65] generalize this approach to two dimensions, allowing axial deformations while still benefitting from significant computational cost reductions.

However, the limitations of symmetry-restricted approaches are inherent to the constraints themselves, as they forbid the emergence of intrinsic shapes such as triaxial or more general octupole-deformed configurations.

2.2.3. Unconstrained coordinate-space (mesh) methods

To overcome the limitations of basis truncation and symmetry constraints, modern HF / HFB solvers have increasingly adopted coordinate-space discretizations, typically based on three-dimensional Cartesian meshes. Notable examples include **MOCCA** [73], **Sky3D** [58], and **HFBFFT** [25]. These codes solve the mean-field equations directly in coordinate space, allowing arbitrary deformations and spontaneous symmetry breaking to emerge naturally.

However, coordinate-space solvers come with their own challenges. High spatial resolution is required to accomodate sufficient numerical accuracy, leading to large three-dimensional grids, thus substantial computational cost. Even with modern resources, fully unconstrained calculations remain computationally intensive, and additional assumptions such as plane reflection symmetry are often introduced to reduce the domain size [72, 73].

Thus, while mesh-based solvers offer maximal flexibility, their computational demands motivate the search for more efficient numerical approaches.

2.2.4. Towards more efficient unconstrained methods

The limitations discussed above highlight the need for methods that combine the flexibility of coordinate-space solvers with improved computational efficiency. In this thesis, we investigate such an approach through the use of the *Generalized Conjugate Gradient* (GCG) method, presented in detail in section 4.2.3. In the HF and energy-density-functional frameworks, the core of the many-body problem reduces to solving a set of single-particle Schrödinger or Kohn-Sham eigenvalue equations, coupled self-consistently through the mean field. These equations must be solved repeatedly during the iterative HF/HFB cycle, and their efficient solution dominates the overall computational cost.

As shown in the present work, applying GCG to the HF single-particle problem provides a promising route towards efficient, symmetry-unrestricted many-body calculations while mitigating the main bottlenecks of fully coordinate-mesh methods.

2.3. Objectives

The aim of this work is to develop a new implementation of the Hartree-Fock method on an unconstrained 3D mesh, by the use of the Generalized Conjugate Gradient method. The goals addressed by this work are the following:

- assess the feasibility of the Generalized Conjugate Gradient for the solution of large-scale eigenvalue problems;
- solve the self-consistent Hartree-Fock equations on an unconstrained 3D mesh;
- verify the numerical accuracy of the new implementation against existing spherical codes;
- gauge the numerical accuracy of deformations, comparing results with well established deformed codes; and
- attempt to produce novel results that specifically require an unconstrained implementaiton of this kind, and establish the advance brought to the field by this work.

2.4. Methods

The methods used in this thesis can be grouped into two main components: the formulation of the energy density functional and the solution of the resulting self-consistent equations.

Skyrme Energy Functional The many-body nuclear problem is approached within the Hartree–Fock framework, described in section 3.1. As discussed in chapter 1, a pure HF treatment is not sufficient for a quantitative description of nuclear structure, and a more general energy density functional (EDF) formulation must be adopted. In this work, we employ the Skyrme EDF, whose construction and resulting mean-field equations are developed in section 3.3. This provides the self-consistent single-particle Hamiltonian that forms the basis for the numerical treatment.

Finite Differences and Generalized Conjugate Gradient Once the equations to solve have been derived, their numerical solution requires both a spatial discretization scheme and an efficient solver for the large-scale eigenvalue problem that arises at each iteration of the self-consistent procedure. Chapter 4 details the methods adopted in this work, starting with the finite-difference discretization of derivatives in section 4.1. The resulting discretized eigenvalue problem is then treated using the GCG method to extract

the relevant low-lying eigenstates, as described in section 4.2.3. Section 4.3 discusses implementation-specific aspects of the code, including convergence criteria, mixing strategies, and the choice of parameters required to ensure stable and efficient minimization of the energy functional.